Spangenberg, E., Heeschen, K., Giese, R., Schicks, J. (2020): “Ester”—A new ring-shear-apparatus for hydrate-bearing sediments. - Review of Scientific Instruments, 91, 6, 064503.

https://doi.org/10.1063/1.5138696

Review of Scientific Instruments

"Ester"—A new ring-shear-apparatus for hydrate-bearing sediments

Cite as: Rev. Sci. Instrum. **91**, 064503 (2020); https://doi.org/10.1063/1.5138696
Submitted: 15 November 2019 . Accepted: 29 May 2020 . Published Online: 19 June 2020

Erik Spangenberg, Katja U. Heeschen, Ronny Giese, and Judith M. Schicks

Review of Scientific Instruments ARTICLE scitation.org/journal/rsi

"Ester"—A new ring-shear-apparatus for hydrate-bearing sediments

Cite as: Rev. Sci. Instrum. 91, 064503 (2020); doi: 10.1063/1.5138696
Submitted: 15 November 2019 • Accepted: 29 May 2020 •
Published Online: 19 June 2020

Erik Spangenberg,[a] Katja U. Heeschen, Ronny Giese, and Judith M. Schicks

AFFILIATIONS

GFZ German Research Centre for Geosciences, Telegrafenberg, D-14473 Potsdam, Germany

[a]Author to whom correspondence should be addressed: erik@gfz-potsdam.de

ABSTRACT

We developed a new thermostated ring-shear-apparatus for investigation on hydrate- or ice-bearing sediments. A fluid inlet at the bottom of the static part of the cell and a fluid outlet at the top of the rotating half-cell allow exchanging and pressurizing the pore fluid in the sample cell to a certain value below the pressure providing the normal load that is applied hydraulically via a seal disk using a syringe pump. The volume change in the sample can be derived from the volume received or injected by the pump. The system allows the use of different methods for the formation and controlled decomposition of hydrate before, after, and during a shear test. The ring-shear-cell is designed for a maximum hydraulic pressure of 30 MPa. A commercial hollow shaft servo actuator applies the torque to the rotating half of the sample cell, and a rotary encoder provides information for determining the shear displacement. Stress path investigations in shear rate controlled experiments with large strain are possible with shear rates up to 12.6 mm/s and torques up to 1440 N m. The system design allows for complex experiments studying the behavior of a shear plane in hydrate- and/or ice-bearing sediments, including the decomposition and reformation of hydrate and/or ice under varying pressure and temperature conditions. It is a useful tool to provide experimental data to support research and engineering in solving problems related to permafrost and hydrate-bearing formations. The system performance is demonstrated by examples of tests on hydrate- and ice-bearing sand samples.

INTRODUCTION

Natural gas hydrates occur worldwide in polar regions, normally associated with onshore and offshore permafrost, and within the sediments of continental and insular margins.[1] The initial estimates from the 1970s and 1980s proposed that the amount of carbon trapped in gas hydrates is greater than the organic carbon bound to all other known reserves together.[2,3] These optimistic estimates and the idea of hydrate as a possible future source of energy have strongly promoted research on methane hydrate.

With currently existing production technologies, only hydrate accumulations in sand reservoirs, where the hydrate fills the pores and hydrate saturation reaches up to 90%,[4–6] can be produced economically.[7] Although the above mentioned estimates are too optimistic[3–9] and the producible hydrate in sands and coarse silts only makes up a small fraction of the overall amount of natural occurring methane hydrate,[3–11] some countries, e.g., Japan and China, push the technology toward commercial production.[12–14]

In addition to the energy aspect of methane hydrate, research interest is also focused on aspects regarding its impact on climate and slope stability.[1,15] Global warming and, hence, ocean warming involve possible destabilization of methane hydrate within the slope sediments along the continental margins, which could result in hazardous slope failure events.[1,16] The methane seepage from the upper continental slope of northwestern Svalbard, for instance, has been attributed to gas hydrate dissociation induced by warming of ambient bottom waters. However, research on this hydrate occurrence that included geochemical drill core analysis revealed that hydrate decomposition started about 8000 years ago when the isostatic rebound induced by the deglaciation of the Barents Sea ice sheet outpaced the eustatic sea-level rise.[17]

Besides the different natural processes that might result in the destabilization of methane hydrate in the slope sediments, human activity associated with the production of hydrocarbons from submarine oil, gas, or gas hydrate reservoirs also affects the surrounding seafloor sediments and might alter their properties and state. For the assessment of the continental slope stability and the risk of slope

failure, especially prior to engineering activities such as the setup of seafloor installations (e.g., pipelines and cables) or drilling for hydrocarbons and their production, knowledge of the geo-mechanical strength properties of the slope sediments and their dependencies on effective stress and hydrate content is essential.

Early measurements of strength properties on hydrate-bearing sediments mainly focused on artificially laboratory-formed hydrate samples,[18–20] because natural samples were rare, expensive to acquire, and strongly biased by core recovery, sample preparation, and sample transformation into the test setup. For early experiments on natural samples, the hydrate stability conditions could not be maintained at all times.[18] However, due to the increasing oil price in this time, more research was undertaken to develop the technology for commercial gas production from natural gas hydrate deposits. The economic interest also powered the development of: (1) core pressure barrels to maintain stability conditions during retrieval of hydrate-bearing sediment cores;[21] (2) core handling systems, which allow transferring the core under *in situ* pressure conditions from the core pressure barrel to storage vessels or analysis systems; (3) core analysis systems for the determination of physical sediment properties at core samples which never left the hydrate stability field. Different systems have been developed and successfully employed during different field campaigns. This includes the integrated Pressure Core Analysis and Transfer systems (PCATS)[22,23] with PCATS-triaxial for strength tests;[24–26] the Pressure Core Characterization Tools (PCCT),[27,28] which is a modular system consisting of a core manipulator, a sub-sampling device, and a number of test chambers like the Direct Shear Chamber (DSC)[27] for direct shear strength tests; and the Pressure Core Non-destructive Analysis Tools (PNATs), which can be used together with the Transparent Acrylic Cell Triaxial Testing (TACTT) system to perform triaxial testing of hydrate-bearing samples under simulated *in situ* conditions.[29,30] The application of these newly developed technologies during a number of hydrate expeditions offshore Japan, India, and China resulted in a strongly increased number of strength tests on natural hydrate-bearing sediment samples.[25,30–34] However, besides hydrate saturation and hydrate distribution, other parameters such as clay content, grain size, distribution, etc. influence the sediment strength properties. For the quantification of the influence of hydrate saturation on the strength properties, the hydrate content needs to be varied and the other influencing parameters have to be kept constant. For this type of systematic study, laboratory investigations on artificial samples are still inevitable. Therefore, we designed a new ring-shear-apparatus for ice- or hydrate-bearing soil samples.

MOTIVATION

The national German gas hydrate project SUGAR (**su**bmarine gas hydrate **r**eservoirs) started in 2008 to investigate possible technologies for gas production from methane hydrate in combination with CO_2 sequestration.[35] The first two funding phases of the project mainly focused on exploration, quantification, reservoir modeling, and production simulation with lab experiments, and the third funding phase of the project investigated possible sites for a gas production test from natural deposits of methane hydrate in the paleo-channel-system of the Danube in the Black Sea.[36,37] Besides a detailed reservoir characterization, an assessment of the geo-mechanical stability of the sediments in the target area was required. Because none of the involved laboratories was equipped with the necessary experimental infrastructure for this type of investigation on hydrate-bearing sediments, one goal was to develop appropriate experimental systems within this funding phase. GEOMAR in Kiel developed a new sophisticated gas hydrate triaxial testing system with a computed tomography (CT) scanner and electrical resistivity tomography (ERT) to investigate the mechanical response of a sample to different production methods, including depressurization and CO_2–CH_4-exchange.[38] The need to understand the mechanical interactions of hydrate with the host sediment and the dependence of macroscopic mechanical sediment behavior on changes and processes at the pore scale triggered the design of testing systems that involve tomographic visualization methods at GEOMAR and other research institutes around the world, e.g., at National Energy Technology Laboratory (NETL, USA) or at Dalian University of Technology (China).[39,40] We focused on developing a system for a straightforward and quick characterization of natural sample material that was expected from the planned drilling campaign in the Romanian sector of the Black Sea Danube deep-sea fan.[41] Besides this, the system should allow studying the influence of artificially formed gas hydrate content on the sediment strength properties. Since no existing system could easily be adjusted for this purpose, we developed a new **e**asy to use ring **s**hear **te**st **r**ig (ESTER). Compared to strength tests using shear boxes and triaxial systems, the advantage of ring-shear-systems is the unrestricted shear displacement, which can be achieved without a reversal in the shear direction.[42] In addition to the determination of peak and residual shear strength, this allows studying the behavior of the sample when the shear plane is fully developed, and hydrate recrystallizes or ice refreezes due to temperature or pressure cycling. This makes this apparatus a useful tool for other research subjects of our institute as well.

APPARATUS DESIGN

An overview of the historical development together with the basic concept of different types of ring-shear- or torsional-shear-systems is given in Bishop *et al.*[42] For any type of torsional- or ring-shear-tests, there is no change in the cross sectional area of the shear plane when the test proceeds and large shear displacements are possible without any reversal in the direction of shear. Besides this, ring-shear-tests show all the disadvantages of the box-shear-tests, such as high local concentration of strain and uncertainty about the direction of principal stresses.[42] Compared to the modern servo-controlled triaxial systems, a ring-shear-setup is relatively simple, cost-efficient, and useful, where large displacements are required for the investigation of the sediment properties.[43] This is of interest for ice- or hydrate-bearing sediments, because during temperature cycling, ice may thaw and hydrate may decompose followed by a reformation of solid ice or hydrate in the pore space. The effect of such a reformation on the sheared sediment can be investigated with this type of system. With the nowadays commercially available servo motor systems, the general buildup of ring-shear-systems allows a very compact design including the pore pressure and temperature regulation system.

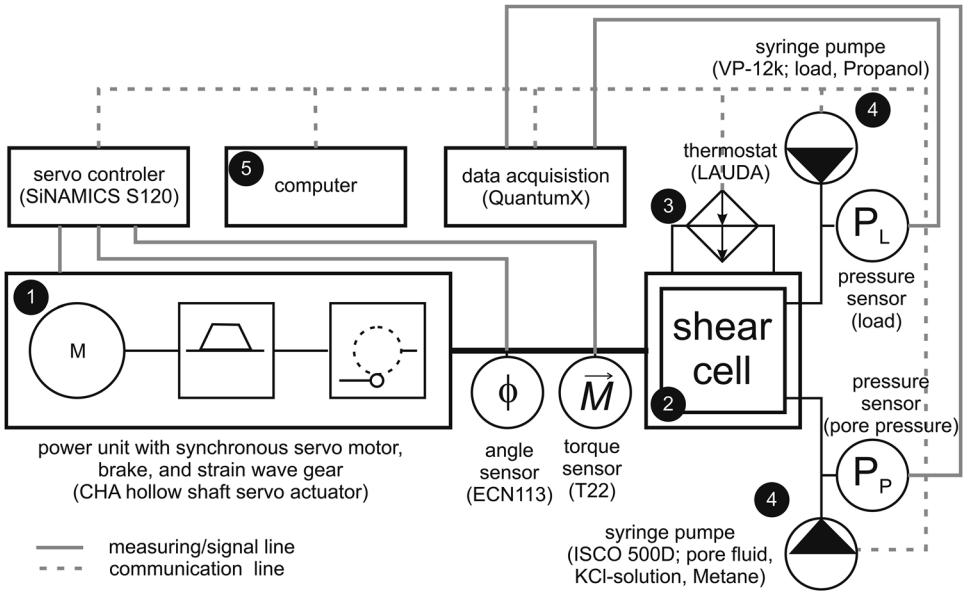

FIG. 1. Scheme of the main components of the ring-shear-apparatus ESTER.

Our system consists of 5 main components illustrated in Fig. 1, which are: (1) a power unit, (2) the ring-shear-cell for hydrate-bearing sediments, which requires (3) a temperature control system and (4) a pressure control system to simulate conditions where hydrate is stable, and (5) a computer for communication with the controllers and the data acquisition system.

Power unit

To generate torsion with sufficient torque and variable angular speed, we chose a hollow shaft servo actuator (CHA series of Harmonic Drive AG), which consists of a synchronous servo motor attached to a strain wave gear with a drive reduction ratio of 160:1 and a resulting maximum torque of M_{Max} = 1840 N m. The maximum output revolution speed is n_{Max} = 19 rpm, and the maximum output brake holding torque is M_{br} = 1440 N m. The servo actuator is connected to a SiNAMICS S120 Servo Controller unit (Siemens). The servo controller is linked to a computer (5) where the controller software allows us to enter the initial settings and to store the sensor readings. The power unit is connected via a torque sensor (HBM T22_1KNM or T22_50NM) and a metal bellows coupling of high torsional rigidity (BKM 1000; R+W Antriebselemente GmbH) to the shear cell. A rotary encoder ECN 113 (Heidenhain GmbH) is also integrated so that in addition to the internal data from the servo actuator, the required measures for the shear test are determined independently behind the output of the power unit.

Ring-shear-cell

The inner diameter of the two-piece ring-shaped sample chamber is d_i = 30 mm, and the outer diameter is d_a = 50 mm. The sample height is about h = 25 mm ± 5 mm. The lower piece of the sample chamber is static and accessible for the pore fluid via a porous ring (Fig. 2). The upper piece rotates driven by the drive shaft, which is connected to the power unit. A PTFE slip ring is placed between the upper and lower halves of the sample cell to decrease internal friction during the shear test (Fig. 2). The internal friction of the system was determined with a water filled cell for pressures of 0.1 MPa–2.5 MPa and shear rates of 0.08 mm/min–4 mm/min. The torque required to overcome the internal friction was determined to be about 3 N m, which is below the range of accuracy given by the manufacturer for the used sensor (1000 N m, ±0.5%). We could not resolve the dependence of internal friction on shear rate or load pressure. Pushers in the rotating and static half of the cell prevent slipping of the

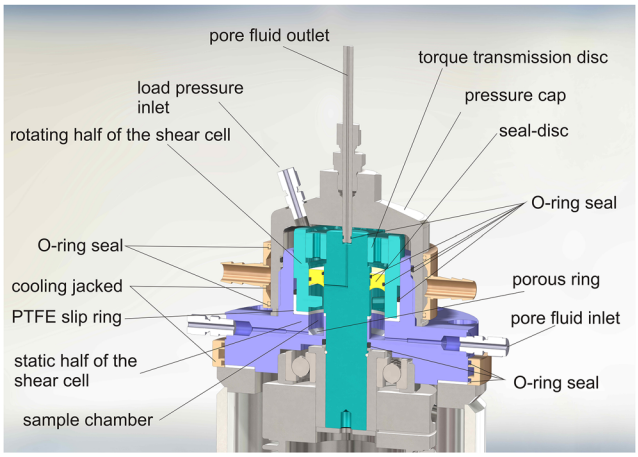

FIG. 2. Cross section through the ring-shear-cell. The static lower half of the cell is shown in blue. The rotating upper half together with the drive shaft and the torque transmission disk is shown in green color. The seal disk, separating the sample from the load pressure system, is shown in yellow.

sample at the cell walls (Fig. 3). A fluid line through the drive shaft into the upper part of the sample chamber allows for a continuous fluid flow through the sample or for exchanging the pore fluid during an experiment. The sample and the pore fluid pressure are separated from the load pressure fluid by a seal disk that acts as the load plate. The pressure fluid provides the normal load via the seal disk to the sample. An O-ring above the PTFE slip ring seals the sample against the load pressure fluid besides the O-ring sealing at the load plate. The pressure cap closes the system to the outside. In order to cool the shear cell containing the sediment sample, cooling jackets are attached to the walls of the pressure cap and the static cell part.

Temperature control system

A Pt100 temperature sensor installed close to the sample in the fluid line of the static half of the shear cell (Fig. 4) provides the necessary external signal for the temperature controller of the LAUDA ECO Silver RE 1050. The LAUDA temperature bath provides a cooling power of 0.6 kW at 0 °C or 0.02 kW at the minimum temperature of −50 °C. The heating power is 2.6 kW, and the maximum working temperature of the bath is 200 °C. The heat transfer fluid (58 vol. % GLYSOFOR N + water; 51 °C freezing point depression) is circulated from the temperature bath through the cooling jackets of the ring-shear-cell. With a standard 19 mm thick Armaflex foam insulation, the cell temperature could be lowered down to about −24 °C. With the use of a GLYSOFOR N water mixture, the maximum temperature is restricted to +80 °C to avoid boiling in the temperature bath. Because there is no temperature information from inside the sample, we work with slow temperature ramps in order to keep temperature gradients low.

The system is able to quickly cool the sample and freeze a certain amount of the saline pore fluid or to keep a constant low temperature to form methane hydrate. Figure 4 shows the temperature curves when the cell is cooled down from room temperature to −6 °C. The temperature difference between the temperature bath and the Pt100 sensor close to the sample gives an idea about the temperature losses between the bath and the sample. Constant sample and bath temperatures indicate that the system has been

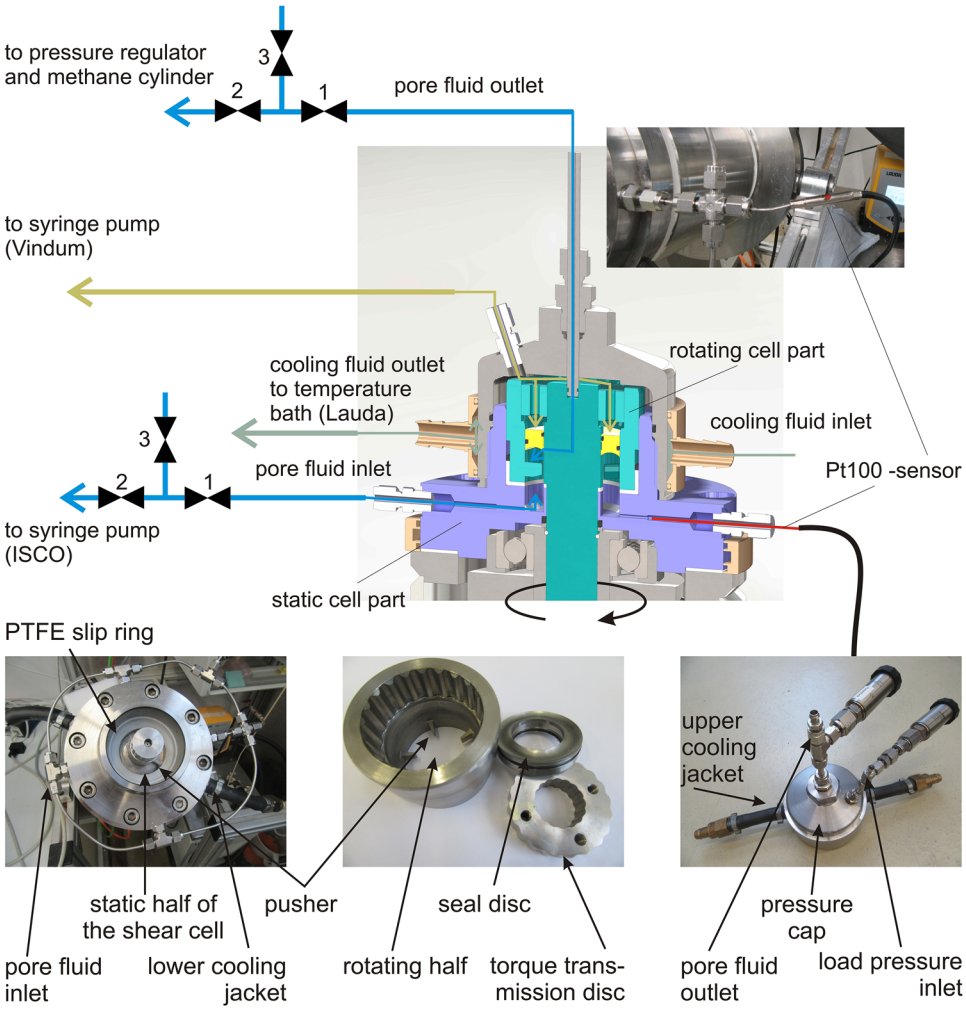

FIG. 3. Sketch of the shear cell and photographs of the main cell components. The sketch shows the connections to the pressure and temperature control systems.

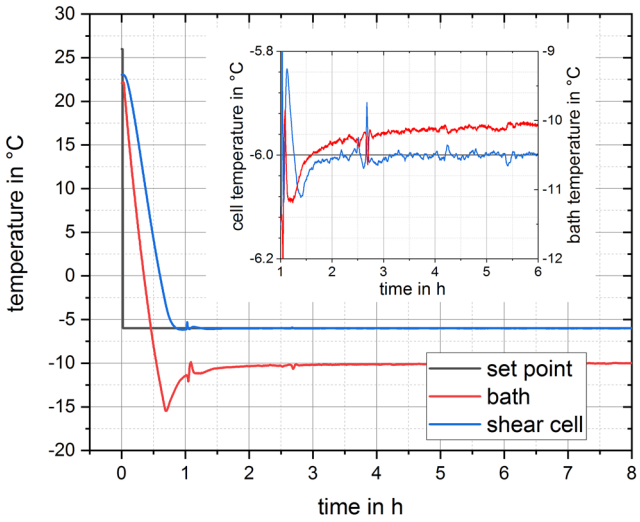

FIG. 4. Cooling curve for an experiment at −6 °C. The Pt100 sensor reaches the set point temperature after less than 2 h. The inserted figure shows that after about 3 h, the temperature fluctuations are clearly below 0.04 °C. The bath temperature still slightly increases, which means that the system is not thermally equilibrated after 3 h.

equilibrated. To be on the safe side, we let the sample equilibrate at constant temperature overnight (12 h–14 h) before performing a shear test.

We always start with the formation of a certain amount of ice in the sediment, even if we aim for the formation of methane hydrate. The ice is transformed into hydrate in a second step. To form a certain amount of ice in the sample, we especially select the salinity and working temperature to keep the influence of temperature variations on the ice content low. For instance, working with a 3% KCl solution at −6 °C produces an ice content of 80% in the sample. If the temperature in the sediment would be higher, at −5.5 °C, compared to −6 °C at the position of the Pt100, the ice content would be 78%. If the temperature in the sample would be lower, at −6.5 °C, the ice content would be 81.5% according to the calculation procedure of Spangenberg *et al.*[44]

Pressure control system

Because methane hydrate requires low temperature and high pressure, a syringe pump ISCO 500D (TELEDYN ISCO) with a maximum pressure of 25 MPa and a pump volume of 500 ml is used to buildup and maintain the necessary constant pore pressure. The pressure, providing the normal load on the sample, is generated with a double cylinder syringe pump VP-12k (Vindum Engineering Inc.) with a cylinder volume of 10 ml and a maximum pressure of 82.7 MPa (12 000 psi). The pressure cap of the setup (Fig. 2) is designed for 30 MPa, which is the pressure limit for the experiments.

The volume which is pumped into or out to keep the load pressure constant during a shear test is recorded together with the pump rate. These data provide the information on sample compaction or dilatation. However, one should keep in mind that initially, at high shear rates, the proportional–integral–derivative (PID) controller of the pump system needs some time to adjust the correct pump rate to keep the pressure constant. Figure 5 shows the pressure and pump rate readings for shear tests on sand samples initially saturated with a 3% KCl solution at −6 °C (80% ice saturation) at two different shear rates. The buildup of shear stress in the sample initially results in a dilatation and a pressure increase in the load pressure fluid above the sample. When the dilatation reaches the maximum, the sample slowly starts to compact again (see also Fig. 8). The upper graph in Fig. 5 shows a situation where the PID controller of the Vindum syringe pump is not fast enough to maintain the pressure close to the set point. The initial dilatation is faster than the pump can adjust the rate to withdraw fluid from the system, which results in an increase in the load pressure above the set point of 0.03 MPa or 1.2%. When the dilatation reaches the maximum value and the sample starts to compact slowly, the controller does not respond fast enough, and the continuing fluid withdraw results in a decrease in the load pressure below the set point of 0.07 MPa or 2.8%. The greatest error in the volume change occurs where the deviation from the set point is the highest. However, the maximum error in the volume change derived from the analysis of the pressure and pump rate data is below 3%. When the controller adjusts the pump rate to keep the pressure constant at the set point, fluid is injected into the cell at a low rate, indicating a slow compaction of the sample. In the lower graph in Fig. 5, the shear rate is just 1/3 of the shear rate for the upper example. The slower deformation process requires lower pump rates to keep the pressure at the set point, which the controller is able to adjust. The cumulative volume pumped into or out of the cell corresponds to the sample compaction or dilatation from which the change in sample height can be calculated (see Fig. 8 in the section titled "Results").

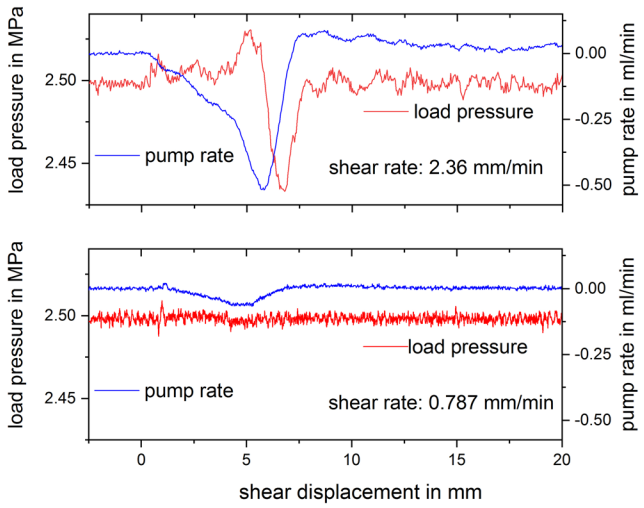

FIG. 5. Pump rate and pressure readings from the Vindum syringe pump as functions of shear displacement for experiments with different shear rates. The upper graph shows that for higher shear rates, the pump controller does not respond fast enough to maintain the pressure exactly at the set point (see explanation in the text).

Data acquisition

The controller software for both syringe pump systems is installed on a computer, so pressure data, flow rates, and total volumes of the syringe pumps can be recorded and stored. In addition to the internal pressure sensors of the pump systems, external sensors for the confining pressure and the pressures at the pore fluid inlet and outlet are installed. These pressure sensors are connected to a QuantumX data acquisition system (HBM) controlled by the "Catman" software (HBM). As mentioned above, the support software for the Siemens SiNAMICS S120 servo controller is also installed on the computer and allows storing and monitoring the readings from the torque sensor and rotary encoder.

EXPERIMENTAL PROCEDURE

The sample chamber is filled with the sediment sample up to a certain level, and the mass of the sample is determined [Fig. 6(a)]. The seal disk is installed to close the sample chamber [Fig. 6(b)]. Depending on the sample handling procedure, the sample below the seal disk can be compacted with careful strokes with a rubber mallet via a plastic ring to protect the surface of the seal disk [Fig. 6(c)]. For the transmission of the momentum from the driver shaft to the upper half of the cell, a toothed torque transmission disk is installed [Fig. 6(d)]. Finally, the volume above the seal disk is filled with the pressure fluid for the load pressure transmission (isopropanol), and the pressure cap is mounted to close the shear cell [Figs. 6(e) and 6(f)]. An O-ring between the static part of the shear cell and the pressure cap (Fig. 3) seals the system.

After sample installation, the ring-shear-cell is connected to the thermostat and the syringe pumps for pressurization. The normal stress or load pressure is applied to the sample surface via the seal disk using a Vindum syringe pump and isopropanol as the pressure liquid. The sample is saturated with a defined KCl solution by injecting the fluid slowly into the bottom of the cell with the ISCO pump. To avoid air bubbles in the sample, the cell is evacuated prior to saturation. Subtracting the volume of the water collected at the pore fluid outlet, the inner volume of the tubing and fluid feed throughs, and the pore volume of the porous ring from the overall injected fluid volume provides the pore volume (V_{pore}) of the sample. The porosity (ϕ) can be estimated using the pore volume, the mass of the dry sand sample (m_s) filled in the cell, and the density of the sand grains, determined with a pycnometer (quartz; $\rho_g = 2.65$ g/cm^3),

$$\phi = \frac{V_{pore}}{V_{pore} + m_s \rho_g}. \quad (1)$$

The first step for the subsequent hydrate formation is the formation of a defined amount of ice. For this purpose, the thermostat is set to a certain temperature below 0 °C depending on the KCl-concentration of the chosen aqueous KCl solution and the amount of ice that should be formed in the sediment. The detailed procedure to form defined amounts of ice from a KCl solution is based on the freezing point depression of salt solutions and published in Spangenberg *et al.*[44] Once the sample in the cell has equilibrated at the targeted temperature, the methane gas cylinder is connected to the fluid outlet, and the brine remaining in the pore network is displaced via the fluid inlet port. When the discharge of brine stops and just gas comes out of the inlet port, the port is closed and the methane pressure is raised deep into the stability field of methane hydrate. The

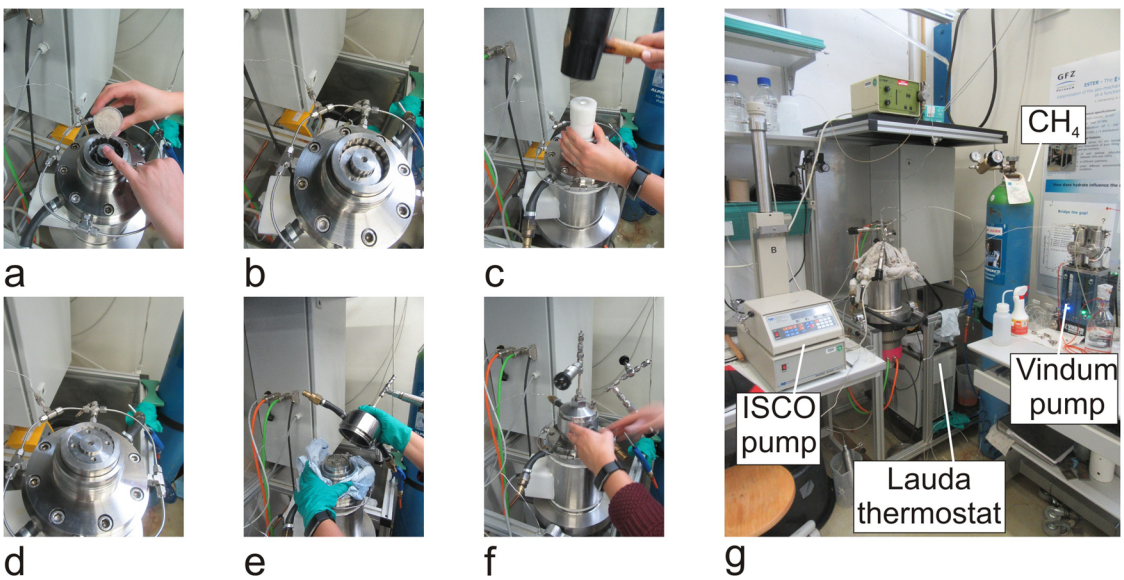

FIG. 6. Installation of a sand sample into the ring-shear-cell ESTER: (a) The fluid line is closed with the finger and sand is filled in the cell. (b) The seal disk is inserted to close the sample chamber (c) The seal disk is pushed to the top of the sample and the sample is compacted. (d) The torque transmission disk is inserted. (e) After filling the volume above the seal disk with isopropanol, the pressure cap is mounted. (f) The pressure cap is screwed down to seal the cell. (g) Overview of the complete system.

temperature is increased slowly over a period of about 24 h to +1 °C. Hydrate will form from the ice and residual brine in the pore space. When the sample has reached the new temperature, the valve to the methane cylinder is closed and the pore pressure is monitored. However, it should be noted that the load pressure has to be adjusted to keep at or below the maximum effective pressure during this procedure to avoid an over-consolidation of the sample. If a constant pore pressure indicates that all ice has transformed into hydrate, the valve to the pressure regulator is opened again. The methane pressure is lowered slightly above the boundary of the hydrate stability, and the pore fluid outlet is closed to the methane cylinder. The KCl solution is again injected into the sample at a pressure slightly above hydrate stability. The amount of injected brine gives a very rough estimate for the reached hydrate saturation, because a part of the injected water will form hydrate with the methane in the pore space. Allowing time for equilibration and recrystallization, one can perform the shear test or perform more cycles of methane injection followed by brine injection to increase the hydrate saturation.

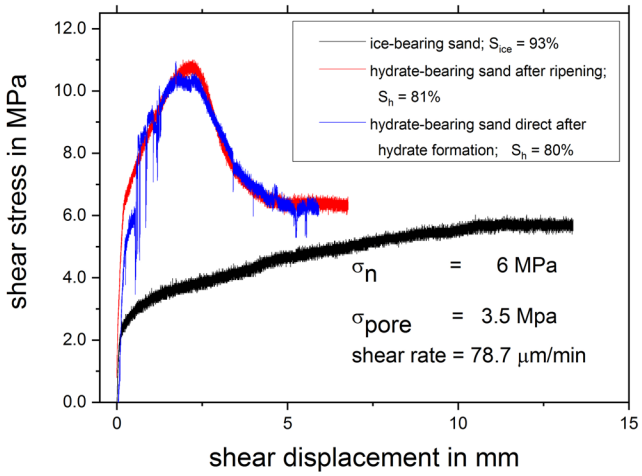

FIG. 7. Shear stress vs shear displacement for hydrate- and ice-bearing sand.

RESULTS

In order to verify the ring-shear-test approach, a number of shear tests on sand, ice-bearing sand, and hydrate-bearing sand have been performed, which will be presented in detail elsewhere. Here, we will present three examples of shear tests on sand (standard filter sand for ground water wells with grain sizes from 0.63 mm to 1.00 mm) used for hydrate formation and production experiments in the **La**rge **R**eservoir **S**imulator (LARS).[45–49] All experiments were carried out with a normal stress of 6 MPa and a pore pressure of 3.5 MPa, where the normal stress and pore pressure were increased in steps to ensure that the effective stress did not exceed 2.5 MPa at any time. For these first experiments, the load pressure was applied with pressurized air, since the Vindum pump was not yet installed. The aim of these first tests was to find out (1) how much hydrate could be formed with the above described method and (2) in which way high contents of ice and hydrate influence the strength properties of the used sand. In addition to these experiments, we present two other examples, measured on a different sand with a wider grain size spectrum (0.1 mm–2 mm; D50 = 0.6 mm), where the volume change was recorded. The experiments have been performed on samples initially saturated with 3% KCl solution at −6 °C (about 80% ice saturation) with a normal stress of 2.5 MPa. All tests have been performed under drained conditions. These experiments demonstrate the influence of the shear rate on the strength of ice-bearing sand.

In the first experiment, the sand was saturated with 1% KCL solution using the ISCO syringe pump. The temperature was set to 0 °C and was decreased with a ramp (0.5 °C/h) to −5 °C to slowly freeze the sample. At this temperature, about 93% of the pore volume is saturated with ice (91.9% ice at −4.5 °C; 93.5% ice at −5.5 °C). The sample was sheared with a rate of 78.7 μm/min or 0.225°/min, which corresponds to a shear strain rate of about $\gamma = 5 \times 10^{-5}$ 1/s. At this shear strain rate, the ice-bearing sample showed ductile behavior with strain hardening (Fig. 7), as was expected from investigations on the rheology of ice, glaciers, and frozen soils in permafrost regions.[50,51]

For the second test, using a freshly prepared sample of the same sand, the temperature was again decreased to −5 °C after the sand sample was saturated with 1% KCl solution. The pore fluid outlet was connected to the methane cylinder, and the methane pressure applied to the sample (hydrate stability pressure at −5 °C is about 2.2 MPa)[45] was slowly increased to 1 MPa. Because of the high ice saturation of 93%, no gas could pass through the sample. Thus, the temperature was increased slowly to about −0.6 °C (ice saturation at this temperature is about 30%), and the remaining brine could be driven out of the sample via the pore fluid inlet by a gentle gas flow. Subsequently, the pore fluid inlet was closed, and both the normal load pressure and the methane pressure were raised stepwise to 6 MPa and 3.5 MPa, respectively, keeping the effective stress always below 2.5 MPa. The temperature was raised slowly to +1 °C during a period of 24 h. Please note that the equilibrium pressure for methane hydrate in contact with methane gas at 1 °C is about 2.85 MPa.[52] The load pressure was lowered to 5.3 MPa, the valve to the methane cylinder was closed, and the pore pressure was monitored. When the pressure remained constant, the pore pressure was lowered to about 3 MPa, and 1% KCl solution was injected slowly via the pore fluid inlet with a restricted flow rate of max 0.1 ml/min to a pore pressure of 3.5 MPa. Because the equilibrium pressure for methane hydrate in 1% KCl solution at 1 °C is 2.93 MPa, the hydrate was stable during the whole injection process.[52] Although we cannot exclude some methane gas entrapped in the hydrate and, thus, not accessible for the brine, we considered the sample to be fully saturated when the flow rate went down to 0 at 3.5 MPa. When closing valves 1 and 2 and opening valve 3 at the pore fluid outlet side, the presence of brine verified that the flow line was not blocked, and the accessible pore volume of the sample was saturated with brine (Fig. 3). The injected 1% KCl solution did form some additional hydrate with the remaining methane. At this point, it should be noted that at 1 °C and 3.5 MPa, hydrate is in equilibrium with a 6.7% KCl solution.[52] About 85% of the water injected with the 1% KCl solution would have to be transformed into hydrate to reach this concentration. This is not possible; with the amount of remaining methane gas, less than 20% of the injected water could be transformed into hydrate.

The procedure was then repeated with the difference that the ISCO pump was set to hydrate equilibrium pressure for the given temperature, and the pressure regulator at the methane cylinder was set to a slightly higher pressure. When the valve to the methane cylinder was opened, methane gas entered the sample and replaced the KCl solution because the ISCO pump received the brine to maintain constant pressure. If the pump had received more than the former injected water volume, the pump would have been stopped and the valves to the cell closed. Gas should be found when opening valve 3 at the pore fluid inlet side. The pore pressure was increased again to 3.5 MPa to transform most of the remaining water in the sample into methane hydrate. We did another two saturation cycles and then stopped the process because the permeability strongly decreased, and it took more than a day to re-saturate the sample with the KCl solution.

After the hydrate formation process, the normal load was increased again to 6 MPa and a shear test was performed. We observed a very irregular curve especially during the strain hardening phase. We did a further experiment with a freshly prepared sample in the exact same way, but at the end of the hydrate formation process, we gave the sample time to equilibrate and recrystallize for one week. The second shear test provided a much smoother curve. We already observed in the LARS experiments that hydrate formed quickly tends to recrystallize and that this process can even change properties such as electrical resistivity.[6] However, both experiments gave the same general trend of strain hardening, about the same peak strength, a comparable strain softening behavior, and about the same post-peak stress level at the end of the test (see Fig. 7). This observed behavior generally agrees with the published triaxial and direct shear test on artificial and natural hydrate-bearing samples.[26,53] The measured peak strength for our samples fits well into the dataset gathered and reviewed by Priest and Hayley.[26] The different behavior of the hydrate-bearing sand samples compared to the ice-bearing sand has been previously observed and results from the fact that according to Durham *et al.*, hydrate is 20 or more times stronger than water ice under the same conditions of temperature and strain rate.[54,55]

The hydrate saturation was determined at the end of the experiment by collecting the methane gas during the depressurization. The hydrate saturation for the first and second experiments was 80.6% and 81.5%, respectively.

The experiments on the other type of sand were carried out with a normal load of 2.5 MPa and a temperature of −6 °C. The samples were saturated initially with a 3% KCl solution, which freezes at −6 °C to form an ice saturation of about 80% (see Fig. 4 and explanation given in the section titled "Temperature Control System"). The tests were performed at considerably higher shear rates of 2.36 mm/min and 0.787 mm/min compared to tests on the hydrate-bearing sands. The shear rates correspond to shear strain rates of $\gamma = 1.57 \times 10^{-3}$ 1/s and $\gamma = 5.25 \times 10^{-4}$ 1/s, respectively. In both tests, we observed strain hardening, a clear peak strength, and post-peak strain softening. These tests were carried out with a different sand and lower ice or higher water content compared to the ice-bearing sample in Fig. 7. In addition to that, the different behavior results also from the higher shear strain rates at which, according to Gold,[50] ice begins to fail brittle. The experiment with the higher shear strain rate in Fig. 8 results in a higher peak strength occurring at larger deformation and in a much stronger sample dilatation. However, the sample dilatation for both experiments shows a maximum at a shear displacement in the post-peak strain softening range, where the slope of the stress curve starts to decrease (Fig. 8; right graph). From this maximum in dilatation, the sample starts to compact slowly with progressing shear displacement. This compaction and the congruent strain softening, observed over a large shear displacement, results from the grinding of quartz grains and the produced frictional heat that might partially melt ice at the shear plane. This interpretation is supported by the observed slight decrease in the bath temperature, necessary to compensate for the produced heat in the sample, and the very fine quartz grains found in the sample after the test.

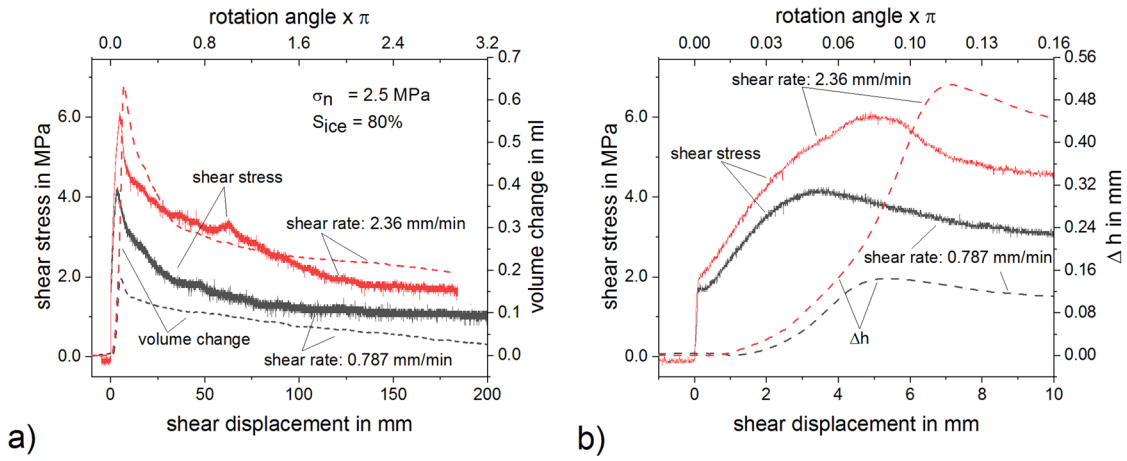

FIG. 8. (a) Shear stress and volume change vs shear displacement for two experiments with different shear rates. (b) Stress response and change in the sample height during the first 10 mm of shear.

DISCUSSION AND CONCLUSIONS

Direct shear tests and ring shear tests are well established and widely used in geotechnics. The new aspect presented here is the *in situ* formation of methane hydrate in the setup prior to the experiment. For a systematic investigation of different factors influencing the shear strength of hydrate-bearing sediments, it is important that experiments conducted under the same conditions will give reproducible results. We were able to show that two experiments using the same sediment pore and load pressure, shear rate, and hydrate saturation using the same hydrate formation method resulted in the same strength parameters. Since the hydrate morphology on a microstructure scale influences the strength,[26] and especially since these influences are of particular interest, we strongly recommend to always follow the same "recipe" when forming the hydrate. Forming hydrate from pore-filling or frame-building ice, as described above, may initially result in different hydrate patterns because the residual pore water will also form hydrate in an "excess-gas" morphology. When methane is injected into the ice-bearing sample to replace the remaining brine, the bound-water wetting the grains will form a fast-grown hydrate-shell with the injected methane when the methane pressure is deep in the hydrate stability field. The formation of grain aligning hydrate in excess-gas systems has been observed with different techniques including microscopy, computed tomography, and synchrotron x-ray computed tomography microscopy.[6,56–58] If water is reinjected, it will form hydrate with the present methane gas in morphologies known from excess-water systems. However, driven by internal gradients in concentration and temperature as well as by Ostwald ripening, the hydrate recrystallizes to more stable structures with less contact with the sand grain skeleton, provided that enough time is given.[59,60] We interpret the "spiky" curve in Fig. 7 as a result of the non-equilibrated internal hydrate morphology.

Owing to the design of the ring-shear-cell with a fluid inlet at the bottom and a fluid outlet at the top of the cell (see Fig. 3), the pore pressure can be changed, a pore fluid flow can be established, and additionally, a fluid exchange can be realized before, during, and after a test. Together with the effective temperature control system, this allows for hydrate destabilization by heating or depressurization, for CO_2–CH_4 exchange in hydrates, and for hydrate reformation after decomposition by pressure increase or temperature decrease. With respect to scientific questions related to the different existing hydrate production approaches, very complex tests are feasible with this apparatus.

The measurements presented in Fig. 7 are carried out at a low shear rate to demonstrate the different behavior of methane hydrate and ice, as already described in the literature (Durham *et al.*).[54,61] Because methane hydrate could be stable below a certain depth within the ice-bearing permafrost, one could expect that the presence of hydrate besides ice could have a significant influence on the resulting mechanical properties. The new system also allows studying these effects.

Liu *et al.* used direct shear tests to study the properties of hydrate-bearing sediments.[53,62] Although they worked with a much higher shear rate, lower normal stress, and lower hydrate saturation, the general dependencies are in good agreement. At about 10% shear strain, the peak shear strength is reached and strain softening is observed. They also showed that a decreasing shear rate results in lower peak strength. The advantage of a ring-shear-system to a direct shear cell with a linear acting shear stress is that large strain can be applied (see Fig. 8). This will allow the study of the influence of different strain rates on the same shear plane or, more generally, the dynamic stress path on a sliding surface.

ACKNOWLEDGMENTS

The authors are very grateful to Thomas Ziegenhagen for supporting the setup of the controller software. The authors thank the staff of the GFZ workshops for their invaluable technical support. The authors also gratefully acknowledge financial support from the German Federal Ministry of Education and Research within the project SUGAR (Research Grant No. 03 G0856C).

DATA AVAILABILITY

The data that support the findings of this study are available from the corresponding author upon reasonable request.

REFERENCES

[1] K. A. Kvenvolden, Rev. Geophys. **31**(2), 173, https://doi.org/10.1029/93rg00268 (1993).
[2] A. V. Milkov, Earth-Sci. Rev. **66**(3-4), 183 (2004).
[3] R. Boswell and T. S. Collett, Energy Environ. Sci. **4**(4), 1206 (2011).
[4] E. Spangenberg and J. Kulenkampff, Geophys. Res. Lett. **33**(24), L24315, https://doi.org/10.1029/2006gl028188 (2006).
[5] R. Boswell, T. S. Collett, M. Frye, W. Shedd, D. R. McConnell, and D. Shelander, Mar. Pet. Geol. **34**(1), 4 (2012).
[6] E. Spangenberg, M. Priegnitz, K. Heeschen, and J. M. Schicks, J. Chem. Eng. Data **60**(2), 258 (2014).
[7] G. J. Moridis, T. S. Collett, R. Boswell, M. Kurihara, M. T. Reagan, E. D. Sloan, and C. Koh, in *Proceedings of the 2008 SPE Unconventional Reservoirs Conference* (Society of Petroleum Engineers, Keystone, Colorado, 2008), Vol. 10, Document ID SPE-114163-MS.
[8] E. B. Burwicz, L. H. Rüpke, and K. Wallmann, Geochim. Cosmochim. Acta **75**(16), 4562 (2011).
[9] E. Piñero, M. Marquardt, C. Hensen, M. Haeckel, and K. Wallmann, Biogeosciences **10**(2), 959 (2013).
[10] R. Boswell, C. Shipp, T. Reichel, D. Shelander, T. Saeki, M. Frye, W. Shedd, T. S. Collett, and D. R. McConnell, Interpretation 4(1), SA13 (2016).
[11] Z. R. Chong, S. H. B. Yang, P. Babu, P. Linga, and X.-S. Li, Appl. Energy **162**, 1633 (2016).
[12] S. Suzuki, S. Sukizaki, Y. Ishihara, I. Yabe, K. Nakata, P. D. Yapa, L. K. Dasanayaka, and U. C. Bandara, in *OCEANS 2008, Quebec City, QC* (IEEE, 2008), pp. 1–4.
[13] Y. Masuda, K. Yamamoto, S. Tadaaki, T. Ebinuma, and S. Nagakubo, Nat. Gas Oil **304**, 285 (2018).
[14] J.-F. Li, J.-L. Ye, X.-W. Qin, H.-J. Qiu, N.-Y. Wu, H.-L. Lu, W.-W. Xie, J. A. Lu, F. Peng, Z.-Q. Xu, C. Lu, Z.-G. Kuang, J.-G. Wei, Q.-Y. Liang, H.-F. Lu, and Kou, Chin. Geol. **1**, 5 (2018).
[15] B. U. Haq, Geol. Soc., London, Spec. Publ. **137**(1), 303 (1998).
[16] T. Mestdagh, J. Poort, and M. De Batist, Earth-Sci. Rev. **169**, 104 (2017).
[17] K. Wallmann, M. Riedel, W. L. Hong, H. Patton, A. Hubbard, T. Pape, C. W. Hsu, C. Schmidt, J. E. Johnson, M. E. Torres, K. Andreassen, C. Berndt, and G. Bohrmann, Nat. Commun. **9**(1), 83 (2018).
[18] W. J. Winters, I. A. Pecher, W. F. Waite, and D. H. Mason, Am. Mineral. **89** (8-9), 1221 (2004).
[19] T. Ebinuma, Y. Kamata, H. Minagawa, R. Ohmura, J. Nagao, and H. Narita, in *Proceedings of Fifth International Conference on Gas Hydrates* (Tapir forlag, Trondheim, Norway, 2005), Vol. 3037, p. 958.

[20]A. Masui, H. Haneda, Y. Ogata, and K. Aoki, in *Proceedings of the 5th International Conference on Gas Hydrates* (Tapir forlag, Trondheim, Norway, 2005), Vol. 2037,
p. 657, TRN: NO0605057
[21]P. J. Schultheiss, T. J. G. Francis, M. Holland, J. A. Roberts, H. Amann, R. J. Parkes, D. Martin, M. Rothfuss, F. Tyunder, and P. D. Jackson, Geol. Soc., London, Spec. Publ. **267**(1), 151 (2006).
[22]P. Schultheiss, M. Holland, J. Roberts, and G. Humphrey, in Proceedings of the 6th International Conference on Gas Hydrates, 2008.
[23]P. Schultheiss, M. Holland, J. Roberts, Q. Huggett, M. Druce, and P. Fox, in *Proceedings of the 7th International Conference on Gas Hydrates (ICGH 2011)* (Hydrafact Ltd., Edinburgh, UK, 2011), p. 17.
[24]P. Schultheiss, J. Roberts, M. Druce, J. Priest, M. Holland, K. Yamamoto, and S. Yang, in Proceedings of the 8th International Conference on Gas Hydrates (ICGH 2014), Beijing, China, 2014.
[25]J. A. Priest, M. Druce, J. Roberts, P. Schultheiss, Y. Nakatsuka, and K. Suzuki, Mar. Pet. Geol. **66**, 460 (2015).
[26]J. A. Priest, J. L. Hayley, W. E. Smith, P. Schultheiss, and J. Roberts, Mar. Pet. Geol. **108**, 424 (2019).
[27]J. C. Santamarina, S. Dai, J. Jang, and M. Terzariol, Sci. Drill. **14**, 44 (2012).
[28]J. Jang, S. Dai, J. Yoneda, W. F. Waite, L. A. Stern, L.-G. Boze, T. S. Collett, and P. Kumar, Mar. Pet. Geol. **108**, 537 (2019).
[29]J. Yoneda, A. Masui, N. Tenma, and J. Nagao, Rev. Sci. Instrum. **84**(11), 114503 (2013).
[30]J. Yoneda, A. Masui, Y. Konno, Y. Jin, K. Egawa, M. Kida, T. Ito, J. Nagao, and N. Tenma, Mar. Pet. Geol. **66**, 451 (2015).
[31]R. Boswell, J. Yoneda, and W. F. Waite, Mar. Pet. Geol. **108**, 143 (2019).
[32]J. Yoneda, A. Masui, Y. Konno, Y. Jin, M. Kida, J. Katagiri, J. Nagao, and N. Tenma, Mar. Pet. Geol. **86**, 1 (2017).
[33]J. Liang, J. Wei, N. Bigalke, J. Roberts, P. Schultheiss, and M. Holland, in *Proceedings of the 9th International Conference on Gas Hydrates* (ICGH, Denver, USA, 2017), Vol. 30, available at geotek.co.uk.
[34]J. A. Priest and J. L. Hayley, J. Geophys. Res.: Solid Earth **124**, 12556, https://doi.org/10.1029/2019jb018324 (2019).
[35]K. Wallmann and J. Bialas, Environ. Earth Sci. **59**(2), 485 (2009).
[36]J. Bialas, I. Klaucke, and M. Haeckel, SUGAR Site Gas Hydrates as a New Energy Source-Reconnaissance of a Pilot Location for the SUGAR Project-Cruise No. MSM34, December 06, 2013-January 16, 2014, Varna, Bulgaria-Varna, Bulgaria, 2014.
[37]K. Schwalenberg, D. Rippe, R. Gehrmann, and S. Hoelz, "Marine CSEM site survey on gas hydrate targets in the Danube delta, western Black Sea," Protokoll über das **26**, 128–213 (2016).
[38]C. Deusner, E. Kossel, N. Bigalke, M. Haeckel, S. Gupta, M. Freise, H. Anbergen, and T. Wille, Energy Geotech. **437-443** (2016).
[39]Y. Seol, L. Lei, J.-H. Choi, K. Jarvis, and D. Hill, Rev. Sci. Instrum. **90**(12), 124504 (2019).
[40]Y. Li, P. Wu, W. Liu, X. Sun, Z. Cui, and Y. Song, Rev. Sci. Instrum. **90**(5), 055106 (2019).
[41]M. Riedel, T. Freudenthal, M. Bergenthal, M. Haeckel, K. Wallmann, E. Spangenberg, J. Bialas, and G. Bohrmann, Mar. Pet. Geol. **114**, 104192 (2020).
[42]A. W. Bishop, G. E. Green, V. K. Garga, A. Andresen, and J. D. Brown, Geotechnique **21**(4), 273–328 (1971).
[43]M. J. Hvorslev, in *Proceedings American Society for Testing and Materials* (American Society for Testing and Materials, Philadelphia, PA, USA, 1939), Vol. 39, p. 999.
[44]E. Spangenberg, K. Seyberth, K. U. Heeschen, M. Priegnitz, and J. M. Schicks, J. Geophys. Res.: Solid Earth **123**(7), 5588, https://doi.org/10.1029/2018jb015855 (2018).
[45]J. M. Schicks, E. Spangenberg, R. Giese, B. Steinhauer, J. Klump, and M. Luzi, Energies **4**(1), 151 (2011).
[46]J. Schicks, E. Spangenberg, R. Giese, M. Luzi-Helbing, M. Priegnitz, and B. Beeskow-Strauch, Energies **6**(6), 3002 (2013).
[47]M. Priegnitz, J. Thaler, E. Spangenberg, C. Rücker, and J. M. Schicks, Rev. Sci. Instrum. **84**(10), 104502 (2013).
[48]M. Priegnitz, J. Thaler, E. Spangenberg, J. M. Schicks, J. Schrötter, and S. Abendroth, Geophys. J. Int. **202**(3), 1599 (2015).
[49]K. U. Heeschen, S. Abendroth, M. Priegnitz, E. Spangenberg, J. Thaler, and J. M. Schicks, Energy Fuels **30**(8), 6210 (2016).
[50]L. W. Gold, J. Glaciol. **19**(81), 197 (1977).
[51]L. U. Arenson, S. M. Springman, and D. C. Sego, Appl. Rheol. **17**(1), 12147–12151 (2007).
[52]R. Sun and Z. Duan, Geochim. Cosmochim. Acta **69**(18), 4411 (2005).
[53]Z. Liu, S. Dai, F. Ning, L. Peng, H. Wei, and C. Wei, Geophys. Res. Lett. **45**(2), 715, https://doi.org/10.1002/2017gl076374 (2018).
[54]W. B. Durham, S. H. Kirby, L. A. Stern, and W. Zhang, J. Geophys. Res.: Solid Earth **108**(B4), 2182, https://doi.org/10.1029/2003jb002534 (2003).
[55]W. J. Winters, W. F. Waite, W. P. Dillon, D. H. Mason, and I. A. Pecher, in 2nd Russian Conference on Geocryology, Russia, 2001.
[56]B. Tohidi, R. Anderson, M. B. Clennell, R. W. Burgass, and A. B. Biderkab, Geology **29**(9), 867 (2001).
[57]M. Chaouachi, A. Falenty, K. Sell, F. Enzmann, M. Kersten, D. Haberthür, and W. F. Kuhs, Geochem., Geophys., Geosyst. **16**(6), 1711, https://doi.org/10.1002/2015gc005811 (2015).
[58]L. Lei, Y. Seol, J.-H. Choi, and T. J. Kneafsey, Mar. Pet. Geol. **104**, 451 (2019).
[59]X. Chen and D. N. Espinoza, Fuel **214**, 614 (2018).
[60]L. A. Stern, S. H. Kirby, and W. B. Durham, Science **273**(5283), 1843 (1996).
[61]L. Lei and Y. Seol, J. Geophys. Res.: Solid Earth **124**, 12430, https://doi.org/10.1029/2019jb018243 (2019).
[62]Z. Liu, H. Wei, L. Peng, C. Wei, and F. Ning, J. Pet. Sci. Eng. **149**, 56 (2017).